Original Paper

Mechanical characteristic and failure mechanism of joint with composite sucker rod

Yan-Wen Zhang [a], Jia-Qi Che [a, *], Han-Xiang Wang [a], Jin Zhang [c], Feng Li [c], Ming-Chao Du [d], Yu-Ting Wang [b]

[a] College of Mechanical and Electronic Engineering, China University of Petroleum (East China), Qingdao, 266580, Shandong, China
[b] National Petroleum Corporation Offshore Engineering (Qingdao) Company Limited, Qingdao, 266520, Shandong, China
[c] Technical Testing Center of SINOPEC, Shengli Oilfield Co., Dongying, 257088, Shandong, China
[d] College of Electrical Engineering and Automation, Shandong University of Science and Technology, Qingdao, 266590, Shandong, China

ARTICLE INFO

ABSTRACT

Composite sucker rods are widely used in oil fields because of light weight, high strength, and corrosion resistance. Bonded technology becomes the primary connection method of composites. However, the joints with composite sucker rods are prone to debone and fracture. The connected characteristics are less considered, so the failure mechanism of the joint is still unclear. Based on the cohesive zone model (CZM) and the Johnson-Cook constitutive model, a novel full-scale numerical model of the joint with composite sucker rod was established, and verified by pull-out experiments. The mechanical properties and slip characteristics of the joint were studied, and the damaged procession of the joint was explored. The results showed that: a) the numerical model was in good agreement with the experimental results, and the error is within 5%; b) the von Mises stress, shear stress, and interface stress distributed symmetrically along the circumferential path increased gradually from the fixed end to the loading end; c) the first-bonded interface near the loading end was damaged at first, followed by debonding of the second-bonded interface, leading to the complete shear fracture of the epoxy, and resulted in the debonding of the joint with composite sucker rod, which can provide a theoretical basis for the structural design and optimization of the joint.

1. Introduction

Composites have the advantages of light weight, high specific strength, good specific stiffness, corrosion resistance, and strong designability, which are increasingly used in the petroleum industry (Li et al., 2022; McIlhagger et al., 2015; Gao et al., 2019). Bonding technology has become the primary connection method between different composites (Demir et al., 2014; Yuan et al., 2004; Shang et al., 2020). However, as shown in Fig. 1, the bonded joint is prone to cohesive degradation, adhesive fracture, and adherent failure. Each of these exerts a detrimental effect on the service life of joints (Bek et al., 2021; Biscaia et al., 2016; Lu et al., 2005). Therefore, it is of great importance to analyze the working characteristics of the joint with the composite suck rod, and identify its failure mechanism to improve the bonding performance.

Researchers have undertaken extensive research on joint performance. For the analysis method for the bonded strength, Kim et al. (2008) proposed a new methodology for failure prediction of single-lap joints (SLJs) considering adherent and adhesive failures. Based on the numerical investigation, the joint strength was determined numerically, and a novel strength improvement method was proposed. Van Dongen et al. (van Dongen et al., 2018; Lapczyk and Hurtado, 2007; Zhang et al., 2015) conducted a blended methodology for progressive damage analysis. Matrix cracks were modeled through the eXtended Finite Element Method (XFEM) and delamination was modeled through the Cohesive Zone Model (CZM). The validation of the mixed approach using open-hole tensile testing demonstrated excellent predictive capability. Hou et al. (Hou et al., 2022; Akpinar and Aydin, 2014; Doitrand et al., 2015) used a multiscale modeling approach to reveal the mechanical behavior of Plain-Woven-Composite (PWC) joints. Combined with Continuum Damage Mechanics (CDM) and CZM,
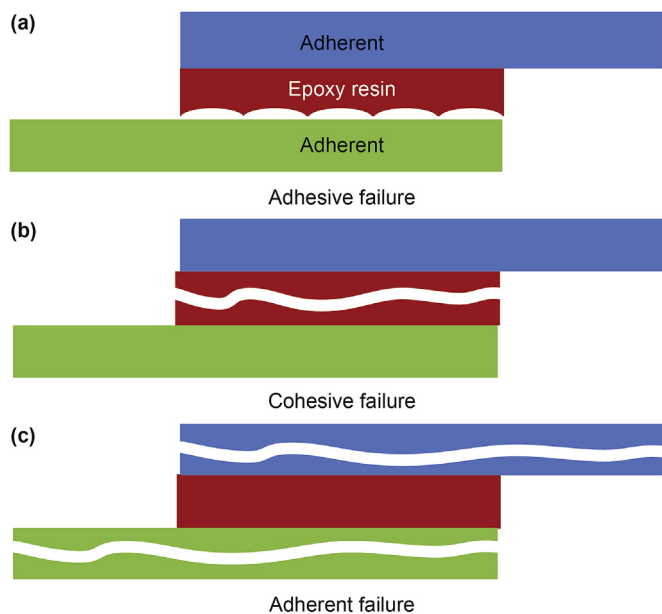
Fig. 1. The failure mode of single lap joint with (**a**) adhesive failure (**b**) cohesive failure and (**c**) adherent failure.

the mechanical behaviors were predicted through the SLJs and double-lap joints (DLJs) under tensile tests. For the effect of structural parameters on bonded strength, Hasheminia et al. (2019) investigated the parameters affecting the joint failure strength by conducting experiments and finite element analysis on SLJs. It is found that failure load increased linearly as the overlap length increased. Aydin et al. (Aydin et al., 2005; Wang et al., 2021) studied the effect of adherent thickness on the failure strength of SLJs by investigating the growth of shear stress relative to different adhesive thicknesses. Reis et al. (2011) studied the influence of adhesive stiffness on the tensile and shear strength of SLJs, and found that an increase of adhesive stiffness would lead to the decrease of joint rotation, which would make the stress distribution more uniform. Kupski et al. (Kupski et al., 2021; Kupski et al., 2019) evaluated the effect of the layups on the quasi-static tensile failure of the joint and found that increasing the bending stiffness of the adherend delayed the onset of damage in joints, but it was no longer effective for final failure. Ozel et al. (Ozel et al., 2014) investigated the mechanical properties of SLJs under tensile load. The results obtained from experimental and numerical analysis showed that composite adherents with different fiber orientation sequences, adherent thicknesses, and overlap lengths affected the failure load and stress distributions. For the bonded performance under complex working conditions, Zhang et al. (Zhang J. et al., 2022; Tanulia et al., 2022; Hafiz et al., 2013; Wu et al., 2021) established the energy-based fatigue life prediction model and realized the accurate prediction of the multiaxial fatigue life based on neural network. Sofia et al. (Teixeira de Freitas and Sinke, 2017; Kang et al., 2007) analyzed the bonded failure between fiber metal laminate (FML) and carbon fiber reinforced polymer (CFRP) under quasi-static load at different ambient temperatures. The interfaces of fracture showed that in I/II mixed mode, the composite mainly break between layers. To sum up, scholars have carried out abundant researches on the analysis method, influencing factors, and failure strength prediction of the joint. However, the research on the joint is generally based on SLJs or DLJs at present, while there is little study on the full-scale joint with CFRP/GFRP composite rods used in oil well, so its mechanical characteristics and failure strength of the joint with multiple wedge grooves are still unclear.

This paper mainly investigated the mechanical properties and

slip characteristics of the joint with composite sucker rod, and explored its failure mechanism by predicting the damage path. The novelties of this paper are: a) based on the CZM and the Johnson-Cook constitutive model, a novel three-dimensional numerical model of the joint with CFRP/GFRP composite sucker rod was firstly established considering the matrix fracture and delamination failure, which was verified by tensile tests; b) the stress distribution and failure stage of the joint with composite sucker rod was revealed for the first time, which can provide a theoretical basis for the structural design and optimization of the joint.

2. Experimental program

2.1. Specimens and material properties

The joint with composite sucker rod was manufactured by Shengli Xinda Composite Material Co., LTD. (Dongying, Shandong). It consists of the steel joint, filled epoxy, and CFRP/GFRP sucker rod as shown in Fig. 2.

Among them, the steel joint is a hollow cylinder with nine wedge-shaped grooves inside 35CrMo alloy steel. It has the advantages of high static strength, fatigue resistance, and impact toughness, making it suitable for impact, bending, torsion, and high-load applications. At the same time, the grooves are filled with single-component epoxy with excellent adhesion, low curing shrinkage, and high stability. The material parameters are shown in Table 1. In addition, the CFRP/GFRP sucker rod with carbon fiber and glass fiber as reinforcement, and multifunctional epoxy as matrix are shown in Fig. 3, which has high tensile strength, light weight, and strong corrosion resistance. The material parameters provided by manufacturer are shown in Table 2.

Before installation, the surface of the sucker rod was polished with sandpaper, and wiped with alcohol. Then the steel joint's inner tapered groove was cleaned. Epoxy was injected into the steel joint, and the CFRP/GFRP sucker rod was inserted. At last, the assembly was placed into an oven at 60 °C for 48 h.

2.2. Experimental method

A customized fixture for the composite sucker rods was made before testing. A pair of wedge-shaped grooves ensured the CFRP/GFRP sucker rod was tightly pressed to the clamp during loading, making the force evenly distributed in the circumferential direction. At the beginning of the experiment, the sample was wiped, and the interface was clamped according to the standard Q/SXD 025—2017. Next, the customized fixture was installed on the end of the CFRP/GFRP sucker rod, ensuring the effective tensile length of the rod was greater than 170 mm. Finally, the assembly was mounted to the tensile machine, aligning the sample axially with the upper and lower fixtures as shown in Fig. 4. The controllable micro-electro-hydraulic servo universal testing machine (WAW-1000F) used to control the displacement of the sample was manufactured by Weihai Shengwei Testing Machine Co., Ltd. according to the standard GB/T 13096-2008 "Pultrusion mechanical properties test method of glass fiber reinforced plastic rod". The loading speed was 5 mm/min. The specimen was loaded continuously until damaged, and the load-displacement curve was recorded with failure mode. The experiment was repeated three times, and the average curve was acquired.

3. Finite element model

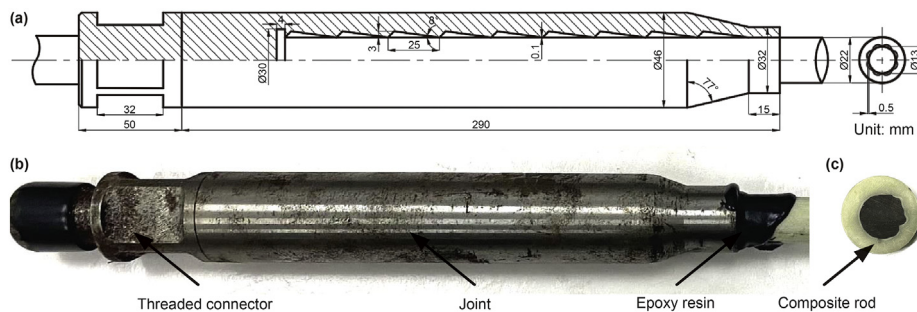### 3.1. Material constitutive model

(1) Damage model for epoxy

Fig. 2. Structure and dimension of joint with (**a**) geometric dimension (**b**) product and (**c**) cross-section rod.

As shown in Fig. 5, it is assumed that the constitutive behavior of the epoxy includes the isotropic stage and elastic-plastic stage (Ma et al., 2022). The linear elastic stage is defined by the elastic modulus E_e. When the element stress reaches the yield strength σ_s, the material enters the elastic-plastic stage. At this time, the yield characteristics of epoxy are described by Johnson-Cook constitutive model. It comprehensively considers the hardening effect, strain rate effect, temperature softening effect, and large deformation at high temperatures of materials under high strain rates. The material parameters of epoxy are listed in Table 3 (Xu et al., 2021). When the strain of elements reaches the equivalent plastic strain ε_p, it is considered that the initial damage of the elements occur, the elastic modulus E_e linearly decrease, and the materials begin to fracture. When the energy exceeds the fracture energy G_{frac}, the material is completely ineffective and the related elements are deleted.

(2) Damage model for interface

According to the actual stress of the engineering structure, *I, II, III* crack or their combinations may appear in the bonded interface.

In the linear elastic stage of the bilinear mixed-mode cohesion model shown in Fig. 6, the damage is assumed to initiate when a quadratic interaction function involving the nominal stress ratios reaches a value of 1, and its basic Eq. (1) is listed as follows.

$$\left(\frac{t_n}{t_n^0}\right)^2 + \left(\frac{t_s}{t_s^0}\right)^2 + \left(\frac{t_t}{t_t^0}\right)^2 = 1 \tag{1}$$

In the formula, t_n, t_s, t_t represent the normal and the shear tractions, MPa. t_n^0, t_s^0, t_t^0 represent the peak values of the nominal stress when the deformation is either purely normal to the interface or purely in the first or the second shear direction, MPa.

In the stage of damage, the damage evolution criterion proposed by Benzeggagh and Kenane (B–K) is used as the damage propagation criterion in the mixed mode in Eq. (2).

$$G_{IC} + (G_{IIC} - G_{IC})\left(\frac{G_{shear}}{G_T}\right)^\eta = G_C \tag{2}$$

Among them,

$$G_{shear} = G_{II} + G_{III}, G_T = G_I + G_{II} + G_{III} \tag{3}$$

In the formula, G_C is the failure equivalent critical fracture energy,

/N·mm. G_I, G_{II}, G_{III} are the fracture energy in *I, II, III* crack type of cohesive model,/N·mm; G_C and G_{IIC} are the critical fracture energy in each direction, /N·mm; η is the damage factor determined by test. The material parameters of the interface are listed in Table 4 (Liu, 2019).

3.2. Geometric model and mesh generation

A three-dimensional finite element model of the joint with CFRP/GFRP sucker rod was established in ABAQUS using the CZM and the Johnson-Cook constitutive model in the explicit integral algorithm. The reduction integral element C3D8R was chosen for steel joints, epoxy, and CFRP/GFRP sucker rod. Furthermore, the mesh size of the steel joint was set at 3 mm, with a count of 2867; meanwhile, the mesh size of the epoxy at 1 mm bears the mesh count setting at 10355. Then, the mesh size of the CFRP/GFRP sucker rod set at 2.5 mm with a count of 3472. In addition, the scanning mesh generation method was used to mesh the whole numerical model with a combination of hourglass control and neutral axis algorithm.

3.3. Contact and constraint

The global contact adopted the finite slip approach. The normal constraint was set to be a hard contact. The tangential constraint was set to a penalty function, and the friction coefficient was set to 0.15. According to Table 4, the tangential constraint was configured as cohesive behavior, and the contact parameters of the epoxy/steel interface as well as the epoxy/composite sucker rod interface were determined.

The global fixed constraint was applied to the right end of the joint. The Y-axis displacement of 5 mm/min was applied to the left end of the composite sucker rod, and the other directions were set as fixed constraints. The finite element model of the joint with composite sucker rod is shown in Fig. 7. The joint's failure progression was simulated by material damage and removing the failure element.

4. Results and discussion

4.1. Load-displacement response

The numerical and experimental load-displacement responses of the joint with composite sucker rod are shown in Fig. 8. The experimental curve shows the brittle failure mode for the joint, which increases linearly until it reached the maximum value of 411 kN at around 4.4 mm, then declined sharply. When the displacement was about 4.8 mm, the force increased slightly from 80 kN to 153 kN, then decreased immediately until the material was completely broken. At the same time, the numerical result was compared to the experimental result and previous simulation
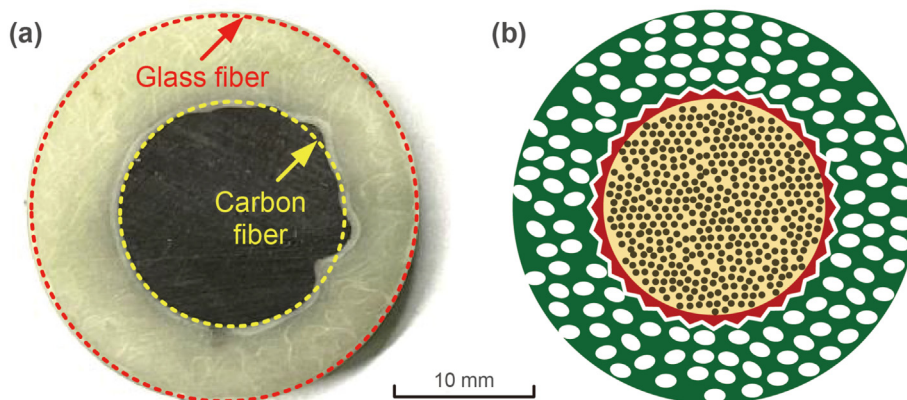
Table 1
Material parameters of bonded joint.

Material	ρ, kg·cm^{-3}	E, MPa	ν
Epoxy	1200	2960	0.38
Steel	7800	216000	0.15

Among them, ρ is density, kg/cm^3; E is elastic modulus, MPa; ν is Poisson's ratio.

Fig. 3. The morphology of composite sucker rod with (**a**) cross-section structure and (**b**) schematic diagram.

Table 2
Material parameters of bonded joint with CFRP/GFRP sucker rod.

Type	ρ, kg·cm^{-3}	E_1, MPa	E_2/E_3, MPa	v_{12}/v_{13}	v_{23}	G_{12}/G_{13}, MPa	G_{23}, MPa
CFRP	1.78	131000	12000	0.324	0.34	5320	3990
GFRP	1.56	53000	14000	0.35	0.36	3710	1670

Among them, ρ is density, kg/cm^3; $E_1/E_2/E_3$ is elastic modulus, MPa; $v_{12}/v_{13}/v_{23}$ is the Poisson's ratio; $G_{12}/G_{13}/G_{23}$ is shear modulus, MPa.
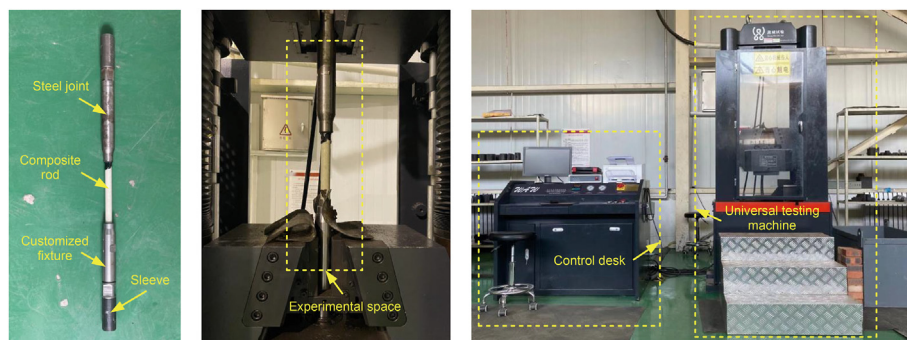

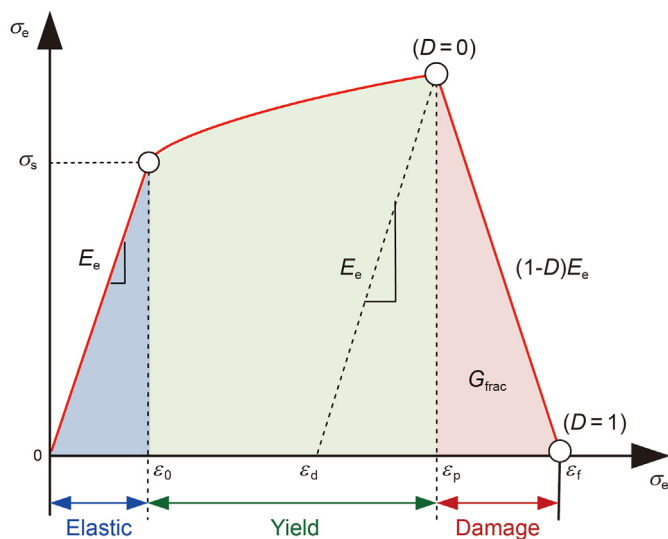**Fig. 4.** Laboratory test of joint with composite sucker rod.

Fig. 5. The constitutive model of epoxy.

Table 3
Material parameters of epoxy.

Model type	Property	Value
Johnson-Cook constitutive model	A	86.23 MPa
	B	144.60 MPa
	N	0.31
	M	0.304
	C	0.124
Damage Model	ε_p	0.05%
Failure Model	G_{frac}	1.1 N/mm

Among them, A, B, n, m, c are parameters of Johnson-Cook model.

method (Zhang Y. et al., 2022). It can be observed that the numerical model in this paper achieved a high degree of agreement in terms of ultimate tensile load, failure displacement, and slope of the curve, which can better represent the elastic and damage behavior of the joint. The predicted tensile load was 392 MPa, with a 5% error, which accords with the precision standards of engineering analysis. An asymmetrical installation error or slips in the customized fixture under the tensile displacement could cause a difference in displacement between the simulation and the experiment.
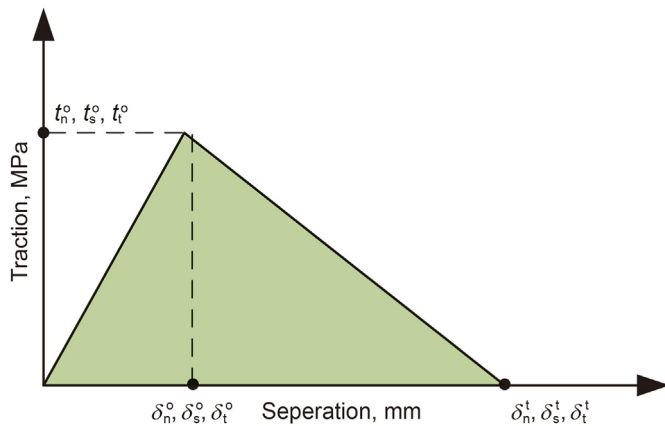
Fig. 6. The constitutive model of interface.

Table 4
Material parameters of interface.

Property	value
t_n, MPa	20
t_s, t_t, MPa	25
G_{IC}, N·mm	0.25
G_{IIC}, N·mm	0.7

4.2. Reaction force and failure mode

The forces of the joint during the process of pulling out include the bonded force, friction resistance force, mechanical locking force at the interface, and shear stress of epoxy.

The bonded force is mainly formed by the interface of epoxy/composite sucker rod and the interface of epoxy/steel joint, which contributes most of the bearing capacity of the joint. At the same time, the friction resistance force is developed between the interface of composite sucker rod/epoxy/steel joint and increased continuously in the joint's elastic process. In addition, the wedge-shaped structure of epoxy provides mechanical locking force at the interface when the composite sucker rod is subjected to axial load. It also exerts an oblique extrusion pressure providing a strong mechanical contact force to resist the axial tensile load. In the end, when the bonded interface fails in pulling out the composite sucker rod, the tensile load needs to overcome the shear stress of epoxy, leading to the cohesive fracture of epoxy.

Fig. 9 shows the failure morphology of the joint with composite sucker rod under different displacements. In the beginning, there was no noticeable change in the joint, and the mechanical fixtures moved relative to each other under the action of external forces. As the axial displacement increased, bond slip occurred and the epoxy glued at the junction was gradually drawn out. Debonding occurs at the end of the joint and the surface of the CFRP/GFRP sucker rod was not damaged. At the same time, the numerical results for the joint's progressive damage with composite sucker rod are illustrated in Fig. 10. The failure process of the joint was divided into four stages including the elastic stage, damage evolution stage, bonded-slip stage, and complete deboned stage as follows.

i. Elastic deformation stage AC (0−4.4 mm)

Fig. 10(a) shows during the initial loading stage (0−0.9 mm), the joint's load grew linearly with increasing displacement. This is due to the tensile load on CFRP/GFRP sucker rod being smaller than the joint's bonded force. Therefore, the joint includes the bonded and static friction force only.

The gradual increase of axial displacement causes the interface between epoxy/composite sucker rod and epoxy/steel joint to degenerate to a certain extent. Axial force acted on the wedge groove and passed through the damaged element from the loading end to the fixed end. The joint reached its tensile strength when the damage path passed through its center. The cementing system was in an elastic coordinated deformation stage due to the small axial displacement, which caused the composite sucker rod's load to increase linearly as shown in Fig. 10(b). The reaction forces at this stage include bonded force, friction resistance force, and mechanical locking force.

ii. Damage evolution stage CD (4.4−4.8 mm)

The further increase of axial load causes the sliding zone to expand to the fixed end. Then, the interface and matrix collapsed violently, and the tensile strength decreased rapidly as shown in Fig. 10(c).

iii. Debonding-slip stage DE (4.8−5.0 mm)

The first interface (epoxy/composite material rod) and second interface (epoxy/steel joint) were almost completely damaged, and the epoxy had been destroyed by shear stress. But the end of the composite sucker rod was still glued to the joint. As the tensile load continues to increase, the composite sucker rod overcomes the bonded force and separated from the steel joint as shown in Fig. 10(d), which takes up a moderate upward in the tensile-displacement curve. The reaction forces at this stage include shear forces in the matrix, bonded forces, friction resistance forces, and mechanical locking forces.

iv. Complete debonding stage E (exceed 5.0 mm)

As the expansion of debonding, elastic and slip zones disappeared, leaving only negligible friction resistance in the joint. This resulted in a significant decline in tensile strength. As the external load continued to load on the composite sucker rod, the friction resistance decreased in proportion to the contact length, resulting in a further reduction of the residual tension until the CFRP/GFRP sucker rod was pulled out completely as shown in Fig. 10(e). The reaction force at this stage includes friction force alone.

4.3. Mechanical characteristic of epoxy

(1) von Mises analysis

The von Mises stress of epoxy along various pathways is determined at the elastic stage to reveal the joint's mechanical property and failure mode, as shown in Fig. 11.

Among them, Fig. 11(a) shows the distribution of von Mises stress along path 1 when tensile displacement changed. Due to the shape of the wedge groove, the stress gradually formed several 'waves' patterns from the fixed to the loading ends, with a peak value of 43.4 MPa at 0.4 mm tensile displacement. With an increase in tensile displacement from 1.2 to 2 mm, the maximum stress of epoxy reached 118.1 and 160.4 MPa respectively. Besides, Fig. 11(b) shows the distribution of von Mises stress along path 2. For the tensile displacement of 0.4 mm, the von Mises stress grew significantly, from 3.6 MPa at the fixed end to 43.4 MPa at 200 mm, then decreased slightly to 21.7 MPa at the loading end. The related fluctuation appeared on the whole curve. As the tensile displacement reached 1.2 and 2 mm, the stress grew synchronously with an
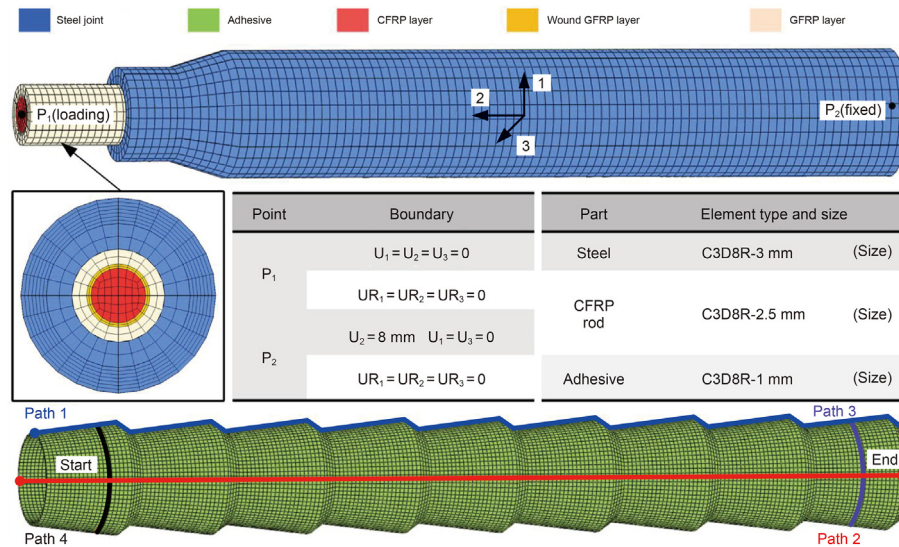
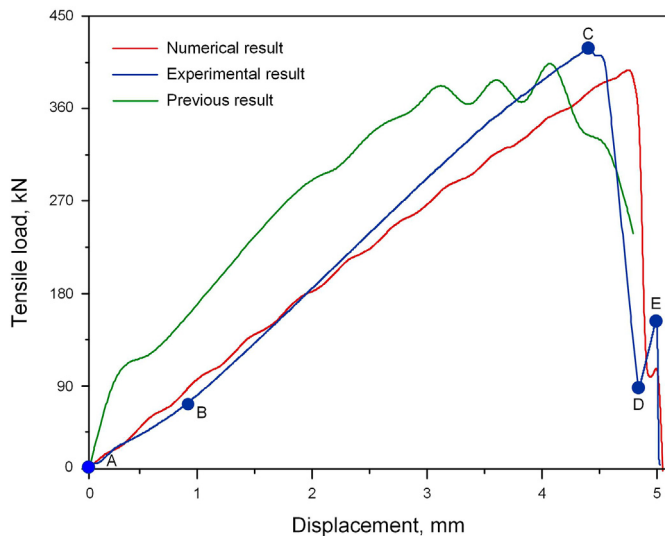**Fig. 7.** Numerical modeling of joint with composite sucker rod.

Fig. 8. The numerical and experimental curve.

increased rate of 170% and 270%, respectively. By comparing Fig. 11(a) and (b), it can be concluded that epoxy's maximum von Mises stress was almost the same on the top and bottom surfaces. The distinction of the von Mises stress at the upper interface changed dramatically because the bottom surface in Fig. 11(b) was a round and smooth surface with more uniform stress distribution. In contrast, due to the wedge-shaped groove on upper surface, the stress on the edge of groove was prone to mutation.

The distribution of von Mises stress near the loading end along path 3 is shown in Fig. 11(c). The graph shows that the von Mises stress was symmetrically distributed along the circumferential path in a 'cross' shape and was divided into four similar parts. The segment of stress curve was molded into 'three peaks' with a high point at the center and a low point on either side. When the tensile displacement increased from 0.4 to 2 mm, the maximum von Mises stress linearly increased from 14.8 to 67.0 MPa. In addition, the distribution of von Mises stress along path 4 near the fixed end is shown in Fig. 11(d). Contrary to the apparent change in stress along path 3, stress distribution along path 4 was more uniform and

almost round at low-stress levels. When the tensile displacement increased from 0.4 to 2 mm, the maximum stress of epoxy resin was 2.0, 5.5, and 8.6 MPa respectively.

(2) Shear stress analysis

The shear stress of epoxy along different paths at the elastic stage is shown in Fig. 12. Among them, Fig. 12(a) presents the distribution of shear stress along path 1 for various tensile displacements. The shear stress increased significantly from the fixed end to loading end and reached maximum value of 20.2 MPa when the tensile displacement 0.4 mm. When the tensile displacement increased from 1.2 to 2 mm, the maximum shear stress of epoxy resin reached maximum values of 55.3 and 75.8 MPa, respectively. Furthermore, Fig. 12(b) shows the distribution of shear stress along path 2. For the tensile displacement of 0.4 mm, the shear stress increased remarkably from 0.8 MPa at the fixed end to 20.2 MPa at about 200 mm and then decreased slightly to 9.0 MPa at the loading end, and related fluctuation appeared in the whole curve. The stress increased synchronously with a rising rate of 174.6% and 275%, respectively, as the tensile displacement reached 1.2 and 2 mm.

Fig. 12(c) illustrates the distribution of shear stress along path 3 near the loading end. As shown in the figure, shear stress was distributed along the axis symmetry of the coordinate. There is a moderate stress mutation at the center of 0−60° between 0 and 90°, and changed dramatically in a bimodal shape with middle low and end high at 60°−90°. When the tensile displacement was 0.4 mm, 1.2 MPa, and 2 mm, the maximum shear stress grew linearly to 11.4, 33.1, and 49.9 MPa, respectively. In addition, Fig. 12(d) shows the distribution of shear stress along path 4. As with path 3, the shear force along the circular cross-section was at a low level and symmetrically distributed along the 0−180° line. Shear stress fluctuated violently between 0° and 180°, forming a double peak with a low middle and high end. When the tensile displacement had increased from 0.4 to 2 mm, the maximum shear stress of epoxy also increased from 0.52 to 1.54 MPa.

(3) Damage progression analysis

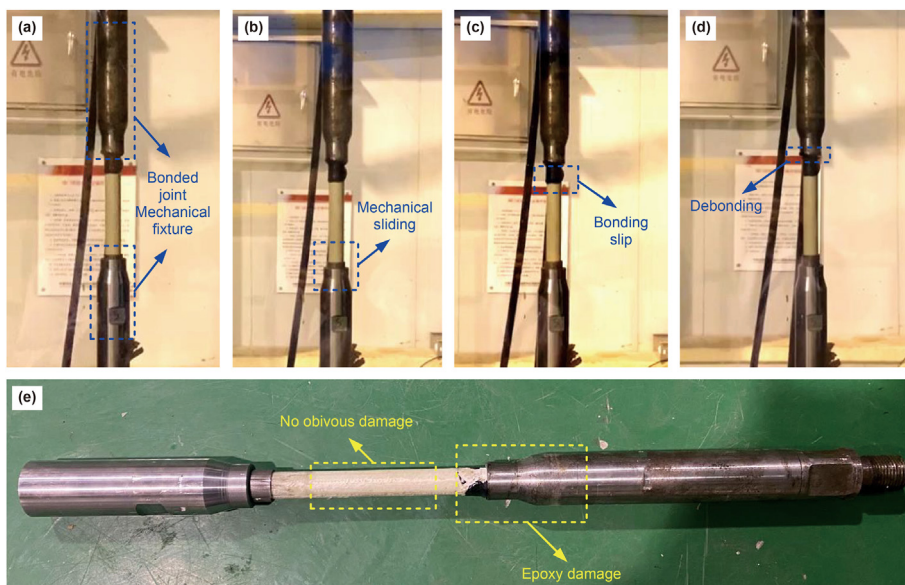The dynamic damage distribution of epoxy in the elastic,

Fig. 9. Failure morphology of joint with composite sucker rod with tensile displacement at (**a**) 0 mm (**b**) 1.1 mm (**c**) 4.4 mm (**d**) 5.0 mm and (**e**) morphology after test.
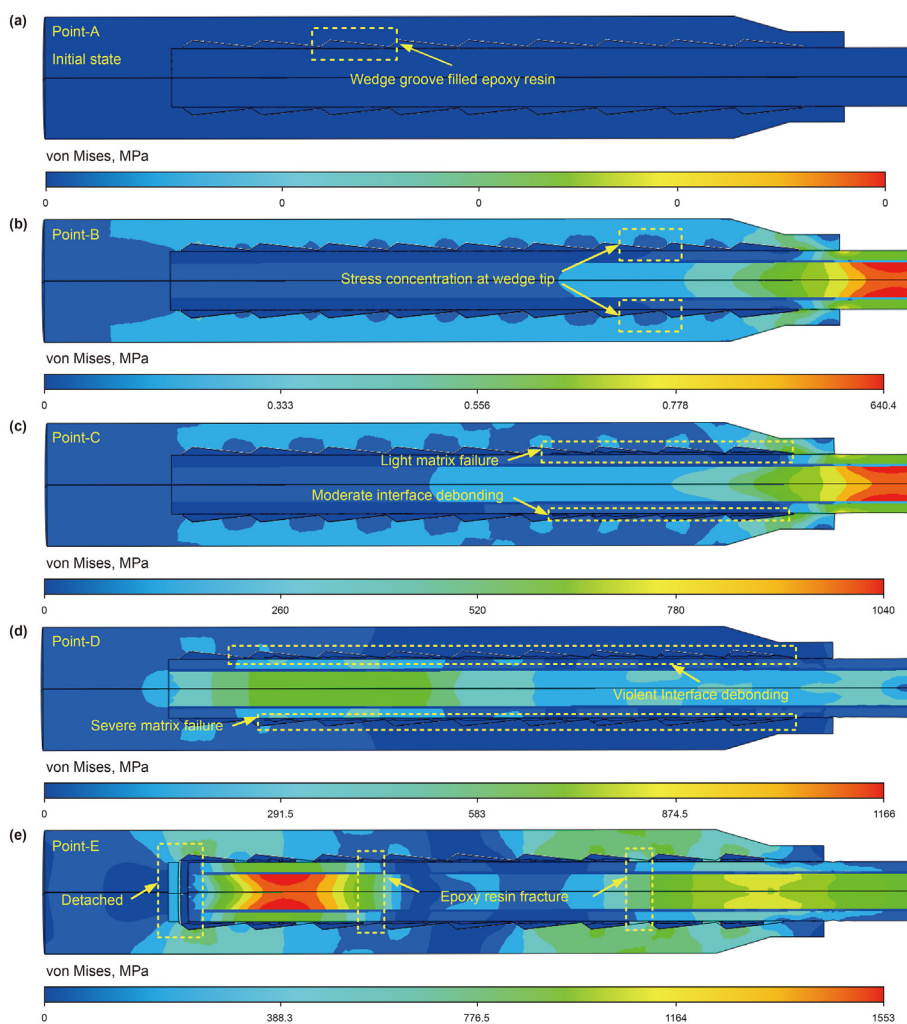

Fig. 10. Numerical failure process of the joint with composite sucker rod with tensile point at (**a**) point A (**b**) point B (**c**) point C (**d**) point D and (**e**) point E.
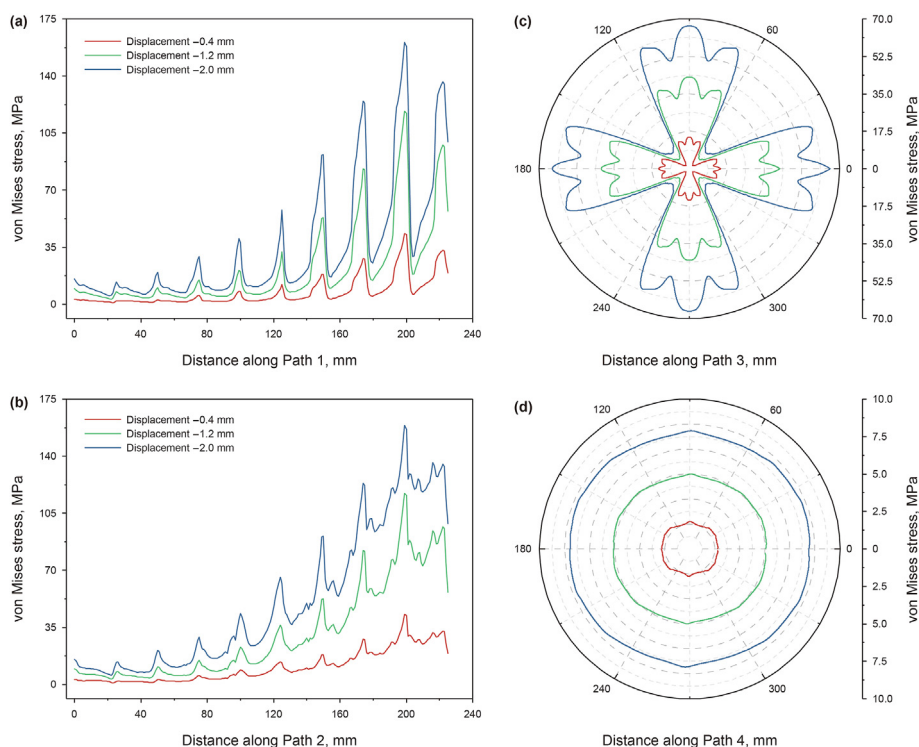
Fig. 11. The distribution of von Mises stress along different path with (**a**) path 1 (**b**) path 2 (**c**) path 3 and (**d**) path 4.

damage evolution, bond slip, and complete debonding stages was examined by the progressive damage method shown in Fig. 13. This was done to investigate the fracture evolution of joint's epoxy. At the same time, the damage parameter DMICRT was selected to represent the element state in epoxy. When the damage factor exceeds 0, the material begins to degrade. When the damage factor is close to 1, the material is irreversibly destroyed and the related elements are removed.

As shown in Fig. 13, when the tensile displacement was 1 mm, and the interfacial bonded force matched the axial tensile load, the epoxy had no apparent visible damage. However, when the tensile displacement reached 3 mm during the elastic stage, a small amount of matrix damage was noticed towards the loading end, which was apparent in the connecting portion of the wedged groove. Three cracks developed unevenly throughout the circumference of the central epoxy. Due to the 4.5 mm tensile displacement at the damage evolution stage, the damage path rapidly stretched towards the fixed end, aggravating the degree of damage in the epoxy, and the corresponding epoxy element was eliminated near the loading end. When the tensile displacement at the bonded-slip stage surpassed 4.8 mm, the epoxy suffered severe damage, resulting in a broad area of irregular fracture. Finally, due to the displacement of 5.6 mm in the stretching direction during the complete peeling stage, the epoxy was split into a plurality of areas in connection position of the wedge-shaped grooves.

4.4. Mechanical characteristics of interface

(1) Peel stress analysis

The interface stress of bonded interfaces along different paths was studied to characterize the contact stress and deboned mechanism of the interface during the bond-slip process, as shown in Fig. 14.

Besides, Fig. 14(a) shows the distribution of interfacial stress between epoxy and steel joints (second-bonded interface) under different tensile displacements. It can be seen that the overall trend of the stress curve was upward, and the sudden change of stress was most evident at the tip of the wedge groove. When the tensile displacement increased from 0.4 to 2 mm, the highest interfacial stress between the composite sucker rod and steel joint reached 19.7, 68.4, and 116.2 MPa, respectively. Meanwhile, Fig. 14(b) shows the distribution of interface stress along path 3 near the loading end. The interface stress was equally distributed throughout the circumferential path in a 'butterfly' shape, which was symmetrical along the straight lines of 0°−180° and 90°−270°. For a single pattern between 0° and 90° with a tensile displacement of 0.4 mm, the stress was relatively high between 0° and 60°, peaking at 0.98 MPa and rapidly decreasing to around 0.32 MPa. With the increase of tensile displacement from 0.4 to 2 mm, the maximum interfacial stress increased linearly from 2.3 to 4.0 MPa.

Under various tensile displacements, the distribution of interfacial tension (the first-bonded interface) between the epoxy resin and composite sucker rod is shown in Fig. 14(c). The curve shows the interface stress in path 2 rocketed from 2.1 MPa at the fixed end to 14.0 MPa at the loading end and fluctuated violently throughout the curve. According to the stress distribution in the displacement of 0.4 mm, when the tensile displacement reached 1.2 and 2 mm, the stress increased synchronously, reaching the peak value of about 44.2 MPa and 69.3 MPa at a rate of 215% and 395%, respectively. Furthermore, Fig. 14(d) illustrates interfacial stress distribution along path 4. The figure demonstrated that the interfacial tension was symmetrically distributed in 'palm' shape along the circumferential path. The stress was concentrated between 60° and 120° at 0.4 mm displacement. Five peaks were evenly distributed in the range of 0.4 MPa. On the contrary, the stress value in the rest interval was almost negligible. The highest interfacial stress increased from 1.6 to 2.9 MPa when the tensile displacement
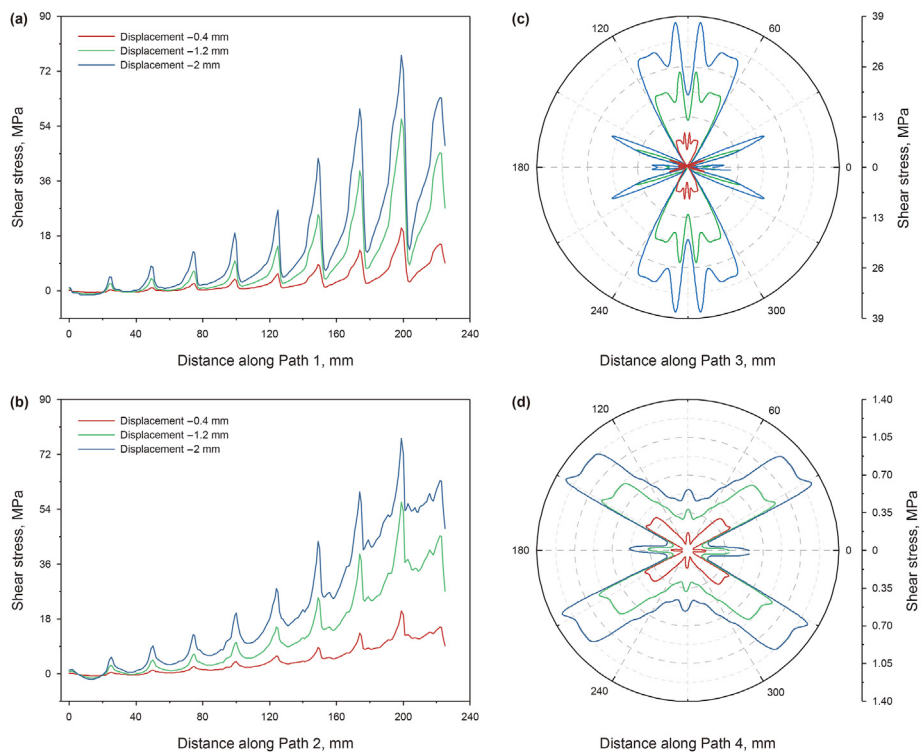
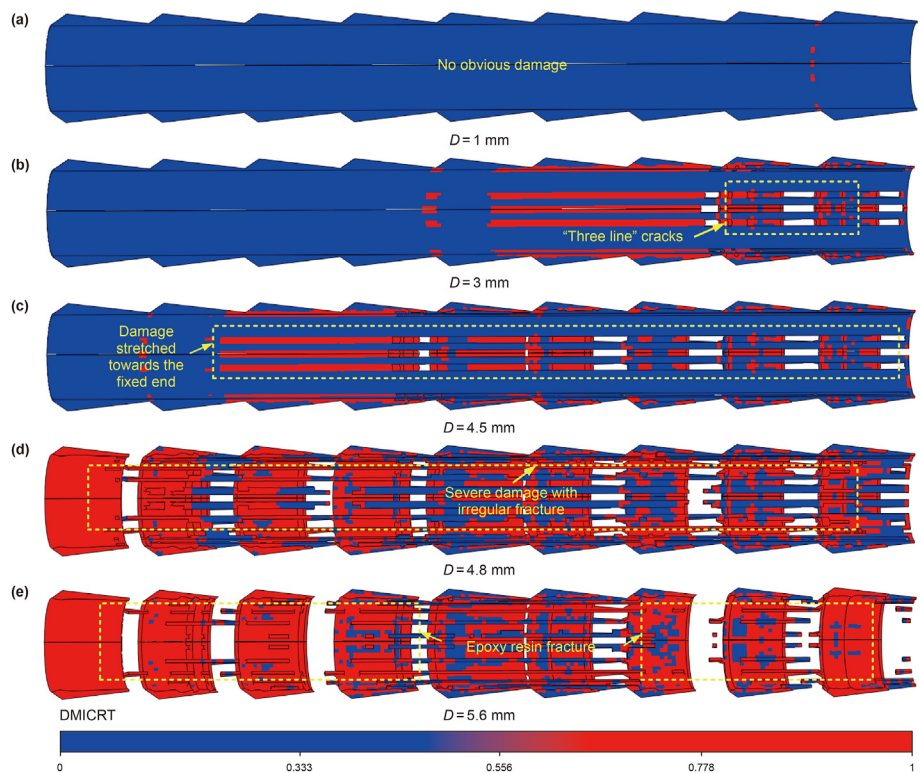**Fig. 12.** The distribution of shear stress along different paths with (**a**) path 1 (**b**) path 2 (**c**) path 3 and (**d**) path 4.

Fig. 13. The dynamic damage distribution of epoxy under different tensile displacement at (**a**) 1 mm (**b**) 3 mm (**c**) 4.5 mm, (**d**) 4.8 mm and (**e**) 5.6 mm.
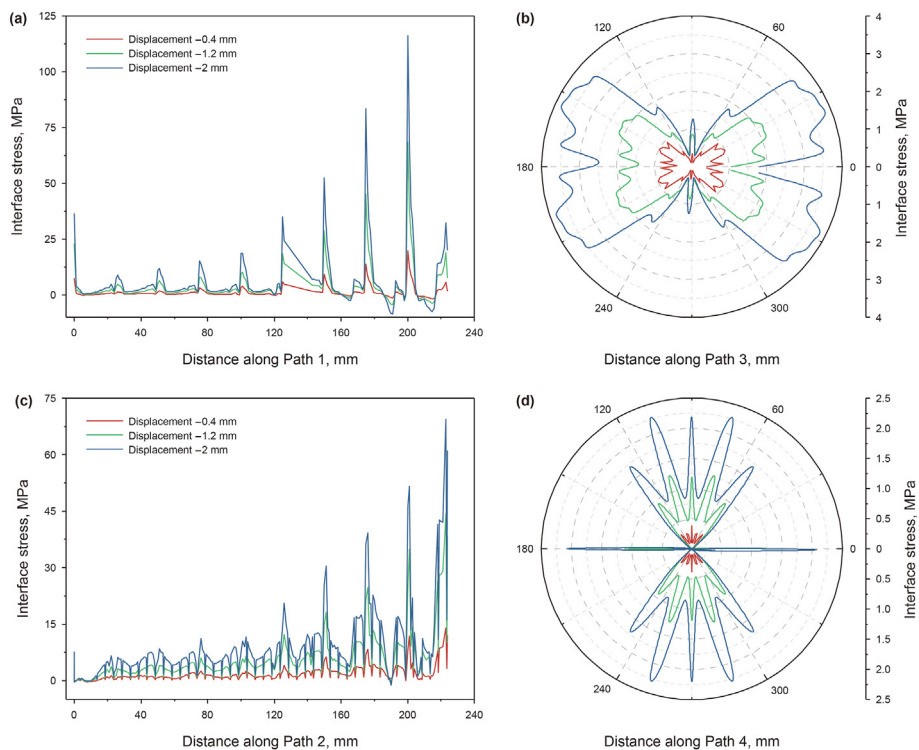
Fig. 14. The distribution of interfacial stress along different path with (**a**) path 1 (**b**) path 3 (**c**) path 2 and (**d**) path 4.

increased from 0.4 to 2 mm.

(2) Damage progression analysis

The progressive damage method was adapted to assess the dynamic damage distribution of epoxy under various tensile displacements. Different axial displacements were used for the elastic,
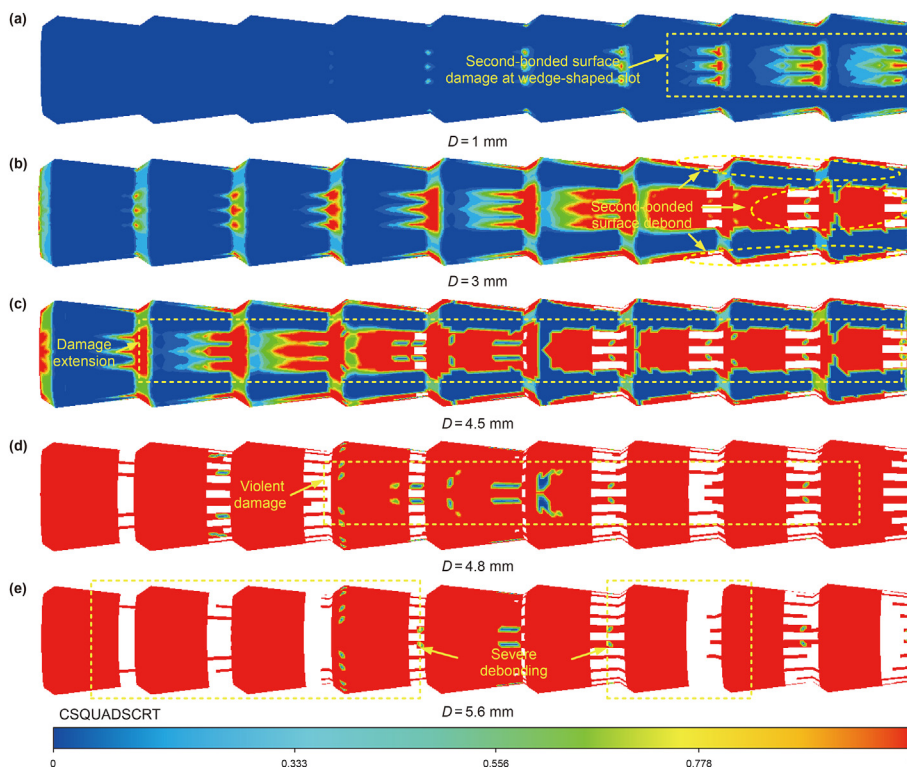

Fig. 15. The dynamic damage distribution of the interface between epoxy and steel joint under different tensile displacements at (**a**) 1 mm (**b**) 3 mm (**c**) 4.5 mm (**d**) 4.8 mm and (**e**) 5.6 mm.
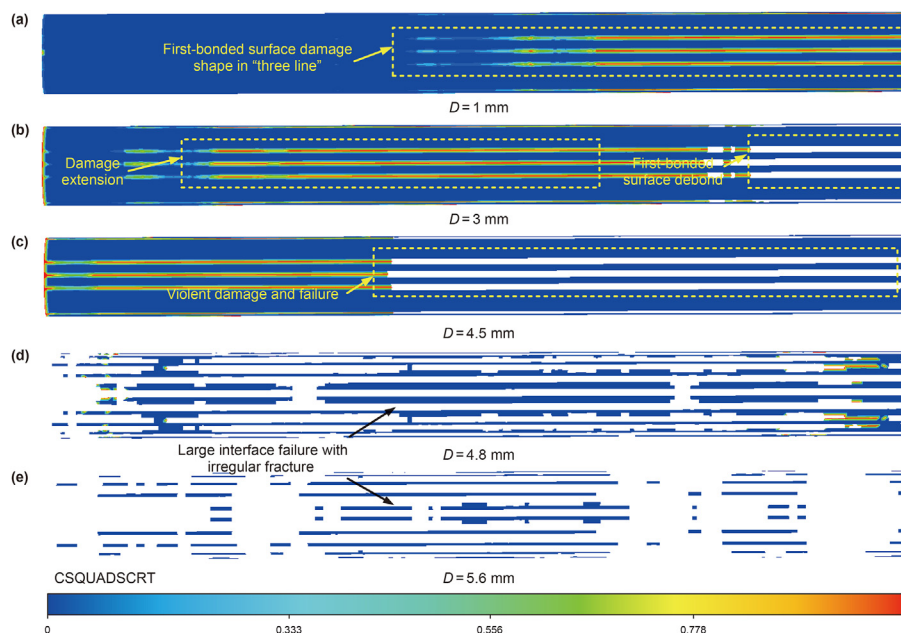
Fig. 16. The dynamic damage distribution of interface between epoxy and composite sucker rod under different tensile displacement at (**a**) 1 mm (**b**) 3 mm (**c**) 4.5 mm (**d**) 4.8 mm and (**e**) 5.6 mm.

damage evolution, bonded-slip, and total debonding stages. The damage parameter CSQUADSCRT was chosen to describe the element state of the interface debonding. When the damage factor exceeded 0, the material began to degrade, and if the value reached 1, the interface became completely deboned.

Fig. 15 shows the distribution of interface damage between epoxy and steel joint (the second-bonded interface) subjected to different tensile displacements. As shown in the figure, when the tensile displacement was 1 mm at the initial elastic stage, the connection position of the wedge-shaped groove near the loading end was damaged. As the displacement increased to 3 mm at a later elastic stage, the bonded interface began to debone unevenly along the circumference, forming a 'three line' shape at center connection position of the wedged groove. The degree of damage to the bonded interface increased violently and synchronously when the tensile displacement was increased to 4.5 mm. The center of the bonded interface towards the loading end became nearly deboned. The debonding path expanded towards the fixed end when the load was increased to 4.8 mm. Large area failure with an irregular fracture of the bonded interface occurred, and only a small portion was linked near the connection position of the wedge groove. Finally, when the tensile displacement exceeded 5.6 mm, severe debonding in the bonded interface occurred, and the interface at the junction of the wedge groove was almost broken.

Fig. 16 shows the damage evolution of the interface between epoxy and the composite sucker rod (the first-bonded interface) under various tensile displacements. As shown in the figure, when the tensile displacement was 1 mm, three 'damage lines' appeared at the middle interface. When the tensile displacement reached 3 mm, the damage path extended to the fixed end, and slight interface damage developed at the loading end. The damage began to run through the main bonded interface as the load was increased to 4.5 mm, forming a 'three line' at the interface center, and eliminating more than half of the bonded interface. When the tensile displacement reached 4.8 mm, considerable debonding developed at the interface, and the primary interface became almost invalid at 5.6 mm of tensile displacement. During the initial axial displacement, the stress is concentrated at the loading end of the epoxy/

composite sucker rod (the first-bonded interface), leading to the first damage and cracking at the interface. As the axial displacements increase, cracks propagate along the first interface. Besides, new cracks began to develop along the interface of epoxy resin/ steel joint (the second-bonded interface) under the wedge groove transition. However, the non-uniform interface deformed the epoxy. When the internal stress in epoxy exceeded the material limits, the matrix fracture started to cause minor damage towards the loading end. As the tensile force increased, the bonded contact nearly separated. Simultaneously, the epoxy was subjected to shear action due to axial displacement. The cracks expanded into the annular area along the lower end of the wedge groove, resulting in epoxy shear damage. The composite sucker rod completely sided through the first-bonded interface as the axial displacement increases, leaving only the friction resistance at the joint to keep it in place.

5. Conclusion

This article established a three-dimensional numerical model of the joint with composite sucker rod based on the CZM and the Johnson-Cook constitutive model, which was validated through pull-out experiments. The mechanical characteristics of the joint was investigated, and the damage evolution was clarified by the progressive damage method. The main conclusions are as follows:

(1) The three-dimensional numerical model of the joint agrees with the experimental results. The predicted tensile load of the joint is 392 MPa with 5% error.
(2) When the tensile displacement is 0.4 mm, the maximum values of von Mises, shear and interface stresses is 43.4, 20.2, and 19.7 MPa, respectively. The maximum values of von Mises and shear stresses increase by about 170% and 27% respectively when the tensile displacement increases from 1.2 to 2 mm. The maximum value of interfacial stress rises even faster, with a growth rate of about 250% and 51%, respectively.

(3) The elastic, damage evolution, bonded-slip, and total debonding stages are used to classify the failure process of the joint with composite sucker rod. As axial displacement increases, the first-bonded interface begins to deteriorate. New cracks begin to appear along the second-bonded interface because of the crack propagation along the first interface. After the interface is close to deboned, the epoxy generates shear damage at the central region as cracks extend into the annular area along the lower end of the wedge groove. The composite sucker rod slides freely along the interface until the CFRP/GFRP composite sucker rod is completely separated from the steel joint.

Statement of originality

The work presented in this paper is, to the best of my knowledge and belief, original, except as acknowledged in the text, and the material has not been submitted, either in whole or in part.

Acknowledgments

References

Akpinar, S., Aydin, M., 2014. 3-D non-linear stress analysis on the adhesively bonded composite joint under bending moment. Int. J. Mech. Sci. 81, 149–157. https://doi.org/10.1016/j.ijmecsci.2014.02.0 24.

Aydin, M., Ozel, A., Temiz, S., 2005. The effect of adherend thickness on the failure of adhesively-bonded single-lap joints. J. Adhes. Sci. Technol. 19 (8), 705–718. https://doi.org/10.1163/1568561054890 499.

Bek, L., Kottner, R., Laš, V., 2021. Material model for simulation of progressive damage of composite materials using 3D Puck failure criterion. Compos. Struct. 259, 113435. https://doi.org/10.1016/j.compstruct.2020. 113435.

Biscaia, H., Borba, I., Silva, C., Chastre, C., 2016. A nonlinear analytical model to predict the full-range debonding process of FRP-to-parent material interfaces free of any mechanical anchorage devices. Compos. Struct. 138, 52–63. https://doi.org/10.1016/j. compstruct. 2015.11.035.

Demir Aydin, M., Akpinar, S., 2014. The strength of the adhesively bonded T-joints with embedded supports. J. Adhesion Adhesives 50, 142–150. https://doi.org/10.1016/j.ijadhadh.2013.12.028.

Doitrand, A., Fagiano, C., Chiaruttini, V., Leroy, F., Mavel, A., Hirsekorn, M., 2015. Experimental characterization and numerical modeling of damage at the mesoscopic scale of woven polymer matrix composites under quasi-static tensile loading. Compos. Sci. Technol. 119, 1–11. https://doi.org/10.1016/j.compscitech.2015. 09. 015.

Gao, L., Zhang, F., Liu, J., Lu, X., Gao, H., 2019. Experimental and numerical study on the interfacial bonding characteristics of FRP-to-concrete joints with mechanical fastening. Construct. Build. Mater. 199, 456–470. https://doi.org/10.1016/j.conbuildmat.2018.12.033.

Hafiz, T., Abdel-Wahab, M., Crocombe, A., Smith, P., 2013. Mixed-mode fatigue crack growth in FM73 bonded joint. Int. J. Adhesion Adhesives 40 (3), 188–196. https://doi.org/10.1016/j.ijadhadh.2012.07.004.

Hasheminia, S., Park, B., Chun, H., Park, J., Chang, H., 2019. Failure mechanism of bonded joints with similar and dissimilar material. Compos. B Eng. 161, 702–709. https://doi.org/10.1016/j.compositesb2018. 11.016.

Hou, Y., Wang, W., Meng, L., Sapanathan, T., Li, J., Xu, Y., 2022. An insight into the mechanical behavior of adhesively bonded plain-woven-composite joints using

multiscale modeling. Int. J. Mech. Sci. 219, 107063. https://doi.org/10.1016/j.ijmecsci.2022.107063.

Kang, S., Kim, M., Kim, C., 2007. Evaluation of cryogenic performance of adhesives using composite-aluminum double-lap joints. Compos. Struct. 78 (3), 440–446. https://doi.org/10.1016/j.compstruct.2005.11.005.

Kim, K., Yi, Y., Cho, G., Kim, C., 2008. Failure prediction and strength improvement of uni-directional composite single lap bonded joints. Compos. Struct. 82 (4), 513–520. https://doi.org/10.1016/j.compstruct.2007.02.005.

Kupski, J., de Freitas, S.T., Zarouchas, D., Camanho, P., Benedictus, R., 2019. Composite layup effect on the failure mechanism of single lap bonded joints. Compos. Struct. 217, 14–26. https://doi.org/10.1016/j.compstruct.2019.02.093.

Kupski, J., de Freitas, S.T., 2021. Design of adhesively bonded lap joints with laminated CFRP adherends: review, challenges and new opportunities for aerospace structures. Compos. Struct. 268, 113923. https://doi.org/10.1016/j.compstruct.2021.113923.

Lapczyk, I., Hurtado, J., 2007. Progressive damage modeling in fiber-reinforced materials. Compos. Appl. Sci. Manuf. 38 (11), 2333–2341. https://doi.org/10.1016/j.compositesa.2007.01.017.

Li, Y., Xiao, Y., Yu, L., Ji, K., Li, D., 2022. A review on the tooling technologies for composites manufacturing of aerospace structures: materials, structures and processes. Compos. Appl. Sci. Manuf. 154, 106762. https://doi.org/10.1016/j.compositesa. 2021.106762.

Liu, Z., 2019. Progressive Damage Failure Behavior of Composite Sucker Rod under Bending Load. China University of Petroleum (Huadong).

Lu, X., Teng, J., Ye, L., Jiang, J., 2005. Bond–slip models for FRP sheets/plates bonded to concrete. Eng. Struct. 27 (6), 920–937. https://doi.org/10.1016/j.engstruct.2005.01.014.

Ma, D., Giglio, M., Manes, A., 2022. Numerical investigation on the uniaxial compressive behavior of an epoxy resin and a nanocomposite. Eur. J. Mech. Solid. 92, 104500. https://doi.org/10.1016/j.euromechsol.2021.104500.

McIlhagger, A., Archer, E., McIlhagger, R., 2015. Manufacturing processes for composite materials and components for aerospace applications. Polym. Compos. Aerosp. Industr. 53–75. https://doi.org/10.1016/b978-0-85709-523-7.00003-7.

Ozel, A., Yazici, B., Akpinar, S., Aydin, M., Temiz, Ş., 2014. A study on the strength of adhesively bonded joints with different adherends. Compos. B Eng. 62, 167–174. https://doi.org/10.1016/j.compositesb.2014. 03.001.

Reis, P., Ferreira, J., Antunes, F., 2011. Effect of adherend's rigidity on the shear strength of single lap adhesive joints. Int. J. Adhesion Adhes. 31 (4), 193–201. https://doi.org/10.1016/j.ijadhadh.2010.12.003.

Shang, X., Marques, E., Carbas, R., Barbosa, A., Jiang, D., da Silva, L., Chen, D., Ju, S., 2020. Fracture mechanism of adhesive single-lap joints with composite adherents under quasi-static tension. Compos. Struct. 251, 112639. https://doi.org/10.1016/j.compstruct.2020. 112639.

Tanulia, V., Wang, J., Pearce, G., Baker, A., Chang, P., Gangadhara Prusty, B., 2022. Experimental and computational assessment of disbond growth and fatigue life of bonded joints and patch repairs for primary airframe structures. Int. J. Fatig. 159, 106776. https://doi.org/10.1016/j.ijfatigue.2022.106776.

Teixeira de Freitas, S., Sinke, J., 2017. Failure analysis of adhesively-bonded metal-skin-to-composite-stiffener: effect of temperature and cyclic loading. Compos. Struct. 166, 27–37. https://doi.org/10.1016/j.compstruct.2017.01.027.

van Dongen, B., van Oostrum, A., Zarouchas, D., 2018. A blended continuum damage and fracture mechanics method for progressive damage analysis of composite structures using XFEM. Compos. Struct. 184, 512–522. https://doi.org/10.1016/j.compstruct.2017.10.007.

Wang, Z., Li, C., Sui, L., Xian, G., 2021. Effects of adhesive property and thickness on the bond performance between carbon fiber reinforced polymer laminate and steel. Thin-Walled Struct. 158, 107176. https://doi.org/10.1016/j.tws.2020.107176.

Wu, G., Li, D., Lai, W., Shi, Y., Kang, H., Peng, Y., Su, X., 2021. Fatigue behaviors and mechanism-based life evaluation on SPR-bonded aluminum joint. Int. J. Fatig. 142, 105948. https://doi.org/10.1016/j.ijfatigue.2020.105948.

Xu, J., Deng, Y., Wang, C., Liang, G., 2021. Numerical model of unidirectional CFRP in machining: development of an amended friction model. Compos. Struct. 256, 113075. https://doi.org/10.1016/j.compstruct.2020.113075.

Yuan, H., Teng, J., Seracino, R., Wu, Z., Yao, J., 2004. Full-range behavior of FRP-to-concrete bonded joints. Eng. Struct. 26 (5), 553–565. https://doi.org/10.1016/j.engstruct.2003.11.006.

Zhang, C., Li, N., Wang, W., Binienda, W., Fang, H., 2015. Progressive damage simulation of triaxially braided composite using a 3D meso-scale finite element model. Compos. Struct. 125, 104–116. https://doi.org/10.1016/j.compstruct.2015.01.034.

Zhang, J., Li, H., Li, Y., 2022. Evaluation of multiaxial fatigue life prediction approach for adhesively bonded hollow cylinder butt-joints. Int. J. Fatig. 156, 106692. https://doi.org/10.1016/j.ijfatigue.2021.106692.

Zhang, Y., Wang, H., Che, J., 2022. Numerical investigation and structural optimization of bonded joints with fiber reinforce plastic sucker rods in offshore reservoirs. J. Adhes. 5, 165–178. https://doi.org/10.1080/00218464.2022.2048822.